*Inorg. Chem.* **2006**, *45*, 5109–5118


# Spin-Gap Formation and Thermal Structural Studies in Reduced Hybrid Layered Vanadates

**Bangbo Yan,[†] Junhua Luo,[†] Paul Dube,[‡] Athena S. Sefat,[‡] John E. Greedan,[‡] and Paul A. Maggard*[,†]**

*Department of Chemistry, 2620 Yarbrough Drive, North Carolina State University, Raleigh, North Carolina 27695-8204, and Department of Chemistry and Brockhouse Institute for Materials Research, McMaster University, Hamilton, ON L8S 4M1 Canada*

Received March 16, 2006

Reduced layered $M(C_4H_4N_2)V_4O_{10}$ ((**I**, M = Co; **II**, M = Ni; **III**, M = Zn); $C_4H_4N_2$ = pyrazine, pyz) hybrid solids were synthesized via hydrothermal reactions at 200–230 °C, and their structures determined by single-crystal X-ray diffraction (*Cmcm*, No. 63, $Z = 4$; $a = 14.311(2)$, 14.2372(4), 14.425(1) Å; $b = 6.997(1)$, 6.9008(2), 6.9702(6) Å; and $c = 11.4990(8)$, 11.5102(3), 11.479(1) Å; for **I**, **II**, and **III**, respectively). All three solids are isostructural and contain $V_4O_{10}^{2-}$ layers condensed from edge- and corner-shared $VO_5$ square pyramids. A single symmetry-unique V atom is reduced by $^1/_2$ electron (on average) and bonds via its apical oxygen atom to interlayer $M(pyz)^{2+}$ chains. Magnetic susceptibility measurements show a strong temperature dependence and a Curie constant that is consistent with two randomly localized spins per $V_4O_{10}^{2-}$ formula for **III**. Further, the unusual discovery of a remarkably well-defined transition to a singlet ground state, as well as formation of a spin gap, is found for **III** at 22(1) K. The temperature-dependent electrical conductivities show apparent activation energies of 0.36 (**I**), 0.46 (**II**), and 0.59 eV (**III**). During heating cycles in flowing $N_2$, the samples exhibit weight losses corresponding to the removal of predominantly pyrazine, pyrazine fragments, and $CO_2$ via reaction of pyrazine with the vanadate layer. The complete removal of pyrazine without loss of crystallinity is found for well-ground samples of **I** and **III**. The SEM images of **I** and **II** after heating at 400–500 °C show relatively intact crystals, but at 600 °C further structural collapse results in the formation of macropores at the surfaces.

## Introduction

The field of metal-oxide/organic hybrid solids has revealed rich new sources of synthetic and structural degrees of freedom to be used in guiding the optimization and expression of physical properties such as ferroelectric, magnetic, or catalytic activity.[1,2] However, among the binary or multinary metal oxides, many intensely investigated ferroelectric and magnetic properties have scarcely, if at all, been manifested in structural forms that utilize the inherent flexibility of organic modifications and functionality. For example, relatively rare and remarkable magnetic phenomena, such as displayed in spin-gap or spin-frustrated systems, are currently underexplored for hybrid oxides/organics with the exception of only a few examples recently reported.[3,4] By contrast, the magnetic behavior of a growing number of metal-oxides/organics has been investigated in many heterometallic molybdate, tungstate, and vanadate families.[5−12] This disparity suggests only a slowly developing ability at

* To whom correspondence should be addressed. E-mail: Paul_Maggard@ncsu.edu.
[†] North Carolina State University.
[‡] McMaster University.

(1) Hagrman, P. J.; Hagrman, D.; Zubieta, J. *Angew. Chem., Int. Ed.* **1999**, *38*, 2638. Hagrman, P. J.; Finn, R. C.; Zubieta, J. *Solid State Sci.* **2001**, *3*, 745.
(2) Forster, P. M.; Cheetham, A. K. *Top. Catal.* **2003**, *24* (1−4), 79.
(3) (a) Lutta, S. T.; Chernova, N. A.; Zavalij, P. Y.; Whittingham, M. S. *J. Mater. Chem.* **2004**, *14*, 2922. (b) Zhang, Y.; Warren, C. J.; Haushalter, R. C.; Clearfield, A.; Seo, D.-K.; Whangbo, M.-H. *Chem. Mater.* **1998**, *10*, 1059.
(4) Shores, M. P.; Bartlett, B. M.; Nocera, D. G. *J. Am. Chem. Soc.* **2005**, *127*, 17986.
(5) Zheng, L.-M.; Wang, X.; Wang, Y.; Jacobson, A. J. *J. Mater. Chem.* **2001**, *11*, 1100.
(6) Devi, R. N.; Rabu, P.; Golub, V. O.; O'Connor, C. J.; Zubieta, J. *Solid State Sci.* **2002**, *4*, 1095.
(7) Khan, M. I.; Yohannes, E.; Nome, R. C.; Ayesh, S.; Golub, V. O.; O'Connor, C. J.; Doedens, R. J. *Chem. Mater.* **2004**, *16*, 5273.
(8) Shan, Y.; Huang, R. H.; Huang, S. D. *Angew. Chem., Int. Ed.* **1999**, *38*, 1751.
(9) Liu, S.; Xie, L.; Gao, B.; Zhang, C.; Sun, C.; Li, D.; Su, Z. *Chem. Commun.* **2005**, 5023.
(10) Maggard, P. A.; Boyle P. D. *Inorg. Chem.* **2003**, *42*, 4250.
(11) Rarig, R. S., Jr.; Lam, R.; Zavalij, P. Y.; Ngala, J. K.; LaDuca, R. L., Jr.; Greedan, J. E.; Zubieta, J. *Inorg. Chem.* **2002**, *41*, 2124.

10.1021/ic0604563 CCC: $33.50 © 2006 American Chemical Society
Published on Web 05/25/2006

successfully targeting specific structural features with the desired electric/magnetic properties for incorporation into flexible organic-containing architectures. Two necessary requirements include both an understanding of the compatibility of oxide/organic species under different reaction conditions (solvent, temperature, etc.), as well as the prevailing structural principles that guide the assembly of specific structures from 'building blocks' in solution.

Our current research involves the synthesis of layered and/or pillared vanadate and perrhenate hybrid solids, as well as the development of the structural principles that direct their formation. The structural principles, based currently on either metal-organic pillaring or charge-density matching, have found importance in the articulation of chirality,[13] open metal sites,[14] optical properties,[15] and for obtaining low-temperature precursors to new metal oxides.[15] The strategy of charge density matching began with the initial synthetic discovery of a metal-segregated layered structure, $Cu(pyz)_2V_6O_{16}\cdot(H_2O)_{0.22(1)}$,[10] containing metal-organic $Cu(pyz)_2^{2+}$ layers and $V_6O_{16}^{2-}$ layers. An analysis of this structure suggested that a matching of the 'charge density' between the metal-organic and metal-oxide layers would be critical in the formation of layered vanadates. As the targeted examples herein, the reduced forms of layered vanadates containing $V^{4+}$ are heavily researched representatives of strongly correlated low-dimensional quantum spin systems, such as found in the $AV_2O_5$ (A = Li, Na, Cs, Mg, and Ca) series of solids.[16] Many such reduced vanadates have attracted considerable interest because of their susceptibility toward spin-Peierl's transitions that lead to spin pairing and nonmagnetic singlet ground states. Examples include the spin-Peierl's transition in $NaV_2O_5$,[17,18] the spin-ladder systems $CaV_2O_5$ and $MgV_2O_5$,[19,20] and spin dimers in $CsV_2O_5$.[21] Thus, the $V_2O_5^{n-}$ ($n = 1-2$) types of layers were targeted as structural units in new hybrid solids in order to allow a greater range of structural modifications in which to study these important spin transitions.

The syntheses and structures of new reduced layered vanadates are reported herein, containing $V_4O_{10}^{2-}$ (i.e., $V_2O_5^{-}$) layers that are intercalated by metal-organic $M(pyz)^{2+}$ layers of chains for M = Co, Ni, and Zn. Their structures and bonding result from the structural matching of $V_4O_{10}$ layers present in $N(CH_3)_4V_4O_{10}$[22] (or more loosely to $NaV_2O_5$) and the $M(pyz)^{2+}$ layers in $Co(pyz)(VO_3)_2$.[5] These new hybrid representatives of reduced layered vanadates are analyzed with respect to their low-dimensional magnetic and electrical properties, as well as for their thermal structural evolution and reactivity under heating.

## Experimental Section

**Materials.** $V_2O_5$ (99.99%, Alfa Aesar), $Co(OH)_2$ (99.9%+, Alfa Aesar), NiO (99.99%+, Alfa Aesar), ZnO (99.99%, Alfa Aesar), and pyrazine (99+%, Alfa Aesar) were used as received. A reagent amount of deionized water was also used in the syntheses.

**Synthesis.** The synthesis of $Co(pyz)V_4O_{10}$ (**I**) was performed by adding $1.86 \times 10^{-1}$ g ($1.02 \times 10^{-3}$ mol) of $V_2O_5$, $3.17 \times 10^{-2}$ g ($3.41 \times 10^{-4}$ mol) of $Co(OH)_2$, $5.46 \times 10^{-2}$ g ($6.82 \times 10^{-4}$ mol) of pyrazine, and 1.228 g ($6.820 \times 10^{-2}$ mol) of $H_2O$ to an FEP Teflon pouch. The pouch was heat-sealed and placed inside a 125-mL Teflon-lined stainless steel reaction vessel which was backfilled with ~42 mL of deionized $H_2O$ before closing. The reaction vessel was heated to 200−210 °C for 24 h inside a convection oven and slowly cooled to room temperature at 6 °C/h. Small black crystals of $Co(pyz)V_4O_{10}$ were obtained in ~50−60% yield, which typically intimately covered an amorphous blue-gray fine powder and/or crystallized on the sides of the Teflon bag. Heating to lower temperatures (160−180 °C) yields the known $Co(pyz)(VO_3)_2$ phase,[5] as determined by powder X-ray diffraction (PXRD). Black crystals of the product were intimately mixed and difficult to mechanically separate from the other unidentified fine powder. Therefore, the entire sample was dispersed in ~30 mL of water and sonicated for 40 min. The water was poured off after allowing the solid products to settle for ~1−2h. This sonication/separation process was repeated three times until a pure sample of $Co(pyz)V_4O_{10}$ was obtained, as judged by PXRD and visually under a microscope.

The synthetic procedures for $Ni(pyz)V_4O_{10}$ (**II**) and $Zn(pyz)V_4O_{10}$ (**III**) involved identical stoichiometric ratios of the starting materials, except for the use of NiO or ZnO in place of $Co(OH)_2$. These reactions were heated to 230 °C for 72 h, and black crystals were obtained in each case in a yield of ~35%. Pure samples of both **II** and **III** were obtained using repeated sonication, which also resulted in an ~10−20% loss of the black crystals, making a determination of the original percent yield difficult to quantify.

**Crystallographic Structure Determination.** A single-crystal data set of **I** was collected on an Enraf-Nonius CAD4-MACH diffractometer operating at 293 K. A suitable black crystal was fixed on a glass fiber using epoxy, and the unit cell determined by a fit of 25 well-centered reflections in the range of $27° < 2\theta < 32°$. The unit cell was measured to be monoclinic with $a = 14.311(2)$ Å, $b = 6.997(1)$ Å, $c = 11.4990(8)$ Å, and $V = 1151.5(3)$ Å$^3$. A unique octant of data ($+h$, $+k$, $+l$) and its Freidel-related octant were collected, while three standard reflections were measured every 80 min of X-ray exposure time. The data were corrected for decay, Lorentz polarization, and absorption effects using $\psi$ scans. The data reduction utilized routines from the NRCVAX suite of programs,[23] and the structure was solved using SIR92[24] in the orthorhombic space group *Cmcm* (No. 63). Hydrogen atoms were introduced at idealized positions and were allowed to ride on the parent carbon


(12) Clemente-León, M.; Coronado, E.; Galán-Mascarós, J.-R.; Giménez-Saiz, C.; Gómez-Garcia, C. J.; Fernández-Otero, T. *J. Mater. Chem.* **1998**, *8* (2), 309.
(13) Yan, B.; Capracotta, M.; Maggard, P. A. *Inorg. Chem.* **2005**, *44*, 6509.
(14) Maggard, P. A.; Yan, B.; Luo, J. *Angew. Chem., Int. Ed.* **2005**, *44*, 2553.
(15) Lin, H.; Yan, B.; Boyle, P. D.; Maggard, P. A. *J. Solid State Chem.* **2006**, *179*, 39.
(16) Ueda, Y. *Chem. Mater.* **1998**, *10*, 2653.
(17) Isobe, M.; Kagami, C.; Ueda, Y. *J. Cryst. Growth* **1997**, *181*, 314.
(18) von Schnering, H. G.; Grin, Yu; Kaupp, M.; Somer, M.; Kremer, R. K.; Jepsen, O.; Chatterji, T.; Weiden, M. *Z. Kristallogr. New Cryst. Struct.* **1998**, *213*, 246.
(19) Bouloux, J. C.; Galy, J. *J. Solid State Chem.* **1976**, *16*, 385.
(20) Bouloux, J. C.; Galy, J. *J. Solid State Chem.* **1976**, *16*, 393. Isobe, M.; Ueda, Y.; Takizawa, K.; Goto, T. *J. Phys. Soc. Jpn.* **1998**, *67*, 755.
(21) Waltersson, K.; Forslund, B. *Acta Crystallogr. Sect.* **1977**, *B33*, 789; Isobe, M.; Ueda, Y. *J. Phys. Soc. Jpn.* **1996**, *65*, 3142.
(22) Zavalij, P. Y.; Whittingham, M. S.; Boylan, E. A. *Z. Kristallogr.* **1996**, *211* (7), 464.
(23) Gabe, E. J.; Le Page, Y.; Charland, J. P.; Lee, F. L.; White, P. S. *J. Appl. Cryst.* **1989**, *22* (4), 384.
(24) Altomare, A.; Cascarano, G.; Giacovazzo, C.; Guagliardi, A. *J. Appl. Crystallogr.* **1993**, *26* (3), 343.

**Table 1.** Selected Crystal and Refinement Data for $M(C_4H_4N_2)V_4O_{10}$ (M = Co, Ni, Zn)

| | | | |
|---|---|---|---|
| empirical formula | $Co(C_4H_4N_2)V_4O_{10}$ | $Ni(C_4H_4N_2)V_4O_{10}$ | $Zn(C_4H_4N_2)V_4O_{10}$ |
| fw | 502.78 | 502.56 | 509.22 |
| space group, *Z* | *Cmcm* | *Cmcm* | *Cmcm* |
| *a*, Å | 14.311(2) | 14.2372(4) | 14.4248(13) |
| *b*, Å | 6.997(1) | 6.9008(2) | 6.9702(6) |
| *c*, Å | 11.4990(8) | 11.5102(3) | 11.4792(10) |
| *V*, Å$^3$ | 1151.5(3) | 1130.85(5) | 1154.16(18) |
| $\mu$ (Mo K$\alpha$), mm$^{-1}$ | 4.59 | 4.88 | 5.22 |
| $d_{calcd}$, g cm$^{-3}$ | 2.90 | 2.95 | 2.93 |
| reflns (total) | 1112 | 1120 | 1142 |
| data/restraints/params | 1112/0/59 | 1120/0/58 | 1142/0/58 |
| GOF | 1.81 | 1.04 | 1.88 |
| final R1($R_f$), wR2[a] ($Rw$) [$I > 2\sigma(I)$] | 0.019, 0.027 | 0.021, 0.060 | 0.036, 0.056 |

[a] $R1 = \sum||F_o| - |F_c||/\sum|F_o|$; $wR2 = \{\sum[w(F_o - F_c)^2]/\sum[wF_o^2]\}^{1/2}$, $w = \sigma_F^{-2}$.

atoms. The structure refinement was performed using a full matrix least-squares based on *F*, with all non-H atoms refining anisotropically, and converged at R1/wR2 = 0.019/0.027 and a GOF = 1.8. A secondary extinction correction was also included in the final cycles of refinement.

Single-crystal data sets of **II** and **III** were collected at 273 and 223 K, respectively, on a Bruker-Nonius ×8 Apex2 diffractometer equipped with a CCD detector and using monochromatized Mo K$\alpha_1$ radiation ($\lambda$ = 0.71073 Å). The crystals were mounted on a 20-$\mu$m nylon loop with a small amount of immersion oil, and the sample temperature maintained using a cold stream of nitrogen from an Oxford Cryosystems 700 Series cryostream cooler. The unit cell dimensions were determined from a symmetry-constrained fit of 6465 reflections within 5.72° < 2$\theta$ < 64.38° for **II** and 8958 reflections within 5.64° < 2$\theta$ < 66.51° for **III**. The data collection strategy involved a combination of $\omega$ and $\varphi$ scans which collected frames up to 2$\theta$ = 67.1° and 67.2° for **II** and **III**, respectively. The frame integration was performed using SAINTPLUS,[25] and the raw data were scaled and corrected for absorption using a multiscan averaging of symmetry-equivalent data using SADABS.[26] The structure of **II** was solved and refined using Bruker SHELXTL,[27] while **III** was solved and refined using the NRCVAX crystallographic program suite.[23] Hydrogen atoms were treated as in **I**. The final structure refinements were performed using a full matrix least-squares based on *F* or $F^2$ and anisotropic refinement of all non-H atoms, which converged to R1/wR2 = 0.021/0.060 and 0.036/0.056 and GOF = 1.0 and 1.9 for **II** and **III**, respectively.

Some data collection and refinement parameters, as well as selected atomic coordinates and isotropic-equivalent displacement parameters, are given in Tables1 and 2. The interatomic distances for selected atom pairs are listed in Table 3. Included in the Supporting Information (CIF) are complete lists of data collection, refinement and anisotropic displacement parameters, and all local interatomic distances and angles for **I**−**III**.

**Electrical and Magnetic Properties.** Magnetic susceptibility measurements were taken using a Quantum Design MPMS XL SQUID magnetometer. The measurements were performed under both zero-field cooled (zfc) and field cooled (fc) conditions. In both cases, the magnetization was measured in the temperature range of 2−300 K at an applied field of 1 kG. Direct-current electrical conductivity measurements were performed on pressed pellets made from well-ground samples. Each pellet was clamped between two metal cylinders and placed into a low-temperature oven for temperature control between 300 and 500 K, and the conductivity measured using a multimeter.

**Table 2.** Selected Atomic Coordinates and Equivalent Isotropic Displacement Parameters (Å$^2$) for $M(C_4H_4N_2)V_4O_{10}$ (M = Co, Ni, Zn)

| atom | site | *x* | *y* | *z* | *U*(eq)[a] |
|---|---|---|---|---|---|
| | | | $Co(C_4H_4N_2)V_4O_{10}$ | | |
| Co | m2m | 0 | 0.3243(1) | 0.75 | 0.0087(4) |
| V | 1 | 0.21251(3) | 0.36479(6) | 0.60329(4) | 0.0093(2) |
| Ol | 1 | 0.2275(2) | 0.3707(3) | 0.4303(2) | 0.016(1) |
| O2 | 1 | 0.1011(1) | 0.3242(3) | 0.6223(2) | 0.0138(9) |
| O3 | m | 0.2585(2) | 0.3824(3) | 0.75 | 0.013(1) |
| Nl | m2m | 0 | 0.0221(7) | 0.75 | 0.016(3) |
| N2 | m2m | 0 | 0.6261(6) | 0.75 | 0.014(3) |
| Cl | m | 0 | 0.9223(7) | 0.8456(4) | 0.048(4) |
| C2 | m | 0 | 0.7266(7) | 0.8475(4) | 0.039(3) |
| | | | $Ni(C_4H_4N_2)V_4O_{10}$ | | |
| Ni | m2m | 0.5 | 0.3161(1) | 0.75 | 0.007(1) |
| V | 1 | 0.2888(1) | 0.3635(1) | 0.6038(1) | 0.008(1) |
| O1 | 1 | 0.4003(1) | 0.3158(2) | 0.6239(1) | 0.011(1) |
| O2 | 1 | 0.2237(1) | 0.1310(1) | 0.5700(1) | 0.013(1) |
| O3 | m | 0.2425(1) | 0.3843(2) | 0.75 | 0.011(1) |
| N1 | m2m | 0.5 | 0.6152(3) | 0.75 | 0.010(1) |
| N2 | m2m | 0.5 | 0.0178(4) | 0.75 | 0.010(1) |
| C1 | m | 0.5 | 0.7157(3) | 0.8484(2) | 0.030(1) |
| C2 | m | 0.5 | 0.9164(4) | 0.6532(2) | 0.039(1) |
| | | | $Zn(C_4H_4N_2)V_4O_{10}$ | | |
| Zn | m2m | 0 | 0.32307(8) | 0.075 | 0.0112(3) |
| V | 1 | 0.2120(1) | 0.36424(6) | 0.6028(1) | 0.0098(2) |
| O1 | 1 | 0.2287(1) | 0.3709 (3) | 0.4302(2) | 0.0168(9) |
| O2 | 1 | 0.1013(1) | 0.3231 (3) | 0.6208(1) | 0.0160(8) |
| O3 | m | 0.2569(2) | 0.3816 (4) | 0.75 | 0.013(1) |
| N1 | m2m | 0 | 0.0193 (6) | 0.75 | 0.014(2) |
| N2 | m2m | 0 | 0.6256 (6) | 0.75 | 0.016(2) |
| C1 | m | 0 | 0.9214 (6) | 0.8441(4) | 0.057(4) |
| C2 | m | 0 | 0.7246 (7) | 0.8457(4) | 0.047(3) |

[a] *U*(eq) is defined as one-third of the trace of the orthogonalized $U_{ij}$ tensor. [b] Hydrogen atoms were constrained to ride on the parent carbon atoms in idealized positions.

**Thermal Structural-Evolution Analyses.** Thermogravimetric analysis (TGA) of each sample was performed on a TGA Q50 analyzer, and the data plotted as the % starting weight versus temperature. The samples were heated to 700 °C at a rate of 5 °C/min under flowing nitrogen or oxygen gas. Post-TGA residues were characterized using PXRD techniques after heating to temperatures of 350, 400, 450, 500, 520, 535, and 550 °C for **I**, and after 700 °C for **I**, **II**, and **III**. PXRD patterns were recorded in transmission mode on an Inel XRG 3000 diffractometer fitted with a CPS 120 position sensitive detector and using Cu K$\alpha_1$ radiation from a sealed-tube X-ray source. In addition, tandem mass spectroscopy/thermogravimetric analysis (TGA−MS) techniques

(25) *SAINT-Plus Ver. 6.22 Data Processing for SMART System*; Bruker Analytical X-ray Instruments, Inc.: Madison, WI, 1995.
(26) Sheldrick, G. M. *SADABS ver. 2.03, Software for Area Detector Absorptions and Other Corrections*; Bruker Analytical X-ray Instruments, Inc.: Madison, WI, 1996.
(27) Sheldrick, G. M. *SHELXTL NT ver. 6.10, Software Package for the Refinement of Crystal* Structures; Bruker Analytical X-ray Instruments, Inc.: Madison, WI, 1998.

**Table 3.** Selected Interatomic Distances (Å) and Bond Valence Analyses[a] in $M(C_4H_4N_2)V_4O_{10}$ (M = Co, Ni, Zn) and $N(CH_3)_4V_4O_{10}$

| atoms | distance | atoms | distance | atoms | distance | atoms | distance |
|---|---|---|---|---|---|---|---|
| | $Co(C_4H_4N_2)V_4O_{10}$ | | | | $Ni(C_4H_4N_2)V_4O_{10}$ | | |
| Co−O2 | 2.062(2) × 4 | Co−N1 | 2.114(5) | Ni−O1 | 2.031(1) × 4 | Ni−N1 | 2.064(2) |
| Co−N2 | 2.112(5) | | | Ni−N2 | 2.058 (2) | | |
| V−O1 | 2.001(2) | V−O2 | 1.634(2) | V−O2 | 2.010(1) | V−O1 | 1.637(1) |
| | 1.898(2) | V−O3 | 1.815(1) | | 1.895(1) | V−O3 | 1.812(1) |
| | 1.903(2) | | | | 1.893(1) | | |
| $\Sigma S_{ij}$ (V) | 4.44[a], 4.67[b] | | | $\Sigma S_{ij}$ (V) | 4.44, 4.68 | | |
| V−V | 3.0370(7) | | | V−V | 3.0438(5) | | |
| | 3.0618(7) | | | | 3.0638(5) | | |
| | 3.3740(7) | | | | 3.3647(3) | | |
| | $Zn(C_4H_4N_2)V_4O_{10}$ | | | | $[N(CH_3)_4]V_4O_{10}$[22] | | |
| Zn−O2 | 2.082(2) × 4 | Zn−N1 | 2.117(4) | V1−O1 | 1.551 | V2−O2 | 1.616 |
| Zn−N2 | 2.109(4) | | | V1−O3 | 1.822 | V2−O3 | 1.764 |
| V−O1 | 1.997(2) | V−O2 | 1.636(2) | V1−O4 | 2.103 | V2−O5 | 2.085 |
| | 1.887(2) | V−O3 | 1.813(1) | V1−O5 | 1.865 | V2−O4 | 1.843 |
| | 1.900(2) | | | | 1.878 | | 1.855 |
| $\Sigma S_{ij}$ (V) | 4.47, 4.70 | | | $\Sigma S_{ij}$ (V1) | 4.78, 5.03 | $\Sigma S_{ij}$ (V2) | 4.75, 5.00 |
| V−V | 3.0259(6) | | | V−V | 3.088 | | |
| | 3.0507(6) | | | | 3.114 | | |
| | 3.3786(6) | | | | 3.405 | | |

[a] $S_{ij} = e^{[(R_o - R)/B]}$ $B = 0.37$, using $R_o = 1.784$ for V(IV).[34,35] [b] $S_{ij} = e^{[(R_o - R)/B]}$ $B = 0.37$, using $R_o = 1.803$ for V(V).

were used for **I** and **II** in order to identify the molecular species that are liberated from the solids during heating. After a room-temperature isotherm of 2 min, each sample was heated to 600 °C at 5 °C/min and the MS spectra of the evolved molecular fragments ($C_4H_4N_2$, $C_3NH_3$, $CO_2$, $O_2$, $N_2$, etc.) were plotted as a function of temperature. Scanning electron microscopy (SEM) of the products was performed on a JEOL JEM 6300 in order to examine the particle morphologies and sizes before and after the heating cycles.

**Electronic Structure Calculations.** Extended Hückel calculations were carried out within the tight-binding approximation[28] using the SAMOA software package.[29] The calculations were performed on $V_2O_9$ and $V_2O_8$ dimers and $V_4O_{16}$ tetramer fragments of **I**−**III**. The atomic orbitals used in the calculations were double-ζ Slater-type orbitals with parameter values identical to those used previously to study the spin interactions in α-$NaV_2O_5$, $CaV_2O_5$, and $MgV_2O_5$.[30]

## Results and Discussion

**Structural Description.** The new $M(pyrazine)V_4O_{10}$ (**I**, M = Co; **II**, M = Ni; **III**, M = Zn) hybrid solids, drawn in Figure 1 for **I**, are isostructural and contain $V_4O_{10}^{2-}$ layers that are bonded and charge-balanced by layers of chains of $M(pyz)^{2+}$. Selected interatomic distances for each structure are given in Table 3. The M atoms bridge between the vanadate layers and are coordinated in an octahedral environment ($MO_4N_2$), with two bonds (cis) to apical oxygen atoms on vanadate layers both above and below (M−O = 2.03−2.08 Å (×4); Ni < Co < Zn) and two to bridging pyrazine ligands (M−N = 2.06−2.12 Å (×2); Ni < Co ∼ Zn). The vanadate layers stack along the *a* axis (×2 per unit cell) with interlayer distances of ∼7.1−7.2 Å for **I**−**III**. The pyrazine ligands bond in a trans fashion to each M atom to form one-dimensional chains down the *b* axis, with neighboring chains offset by ∼2.5 Å. Each pyrazine occupies a relatively large cavity of 6.9 × 7.0 Å, Figure 1a, and leads to the relatively larger thermal displacement parameters of C atoms in the *a*-axis direction in all three structures. Alternate trial structural refinements and difference Fourier maps do not indicate these are split positions or multiple ligand orientations.

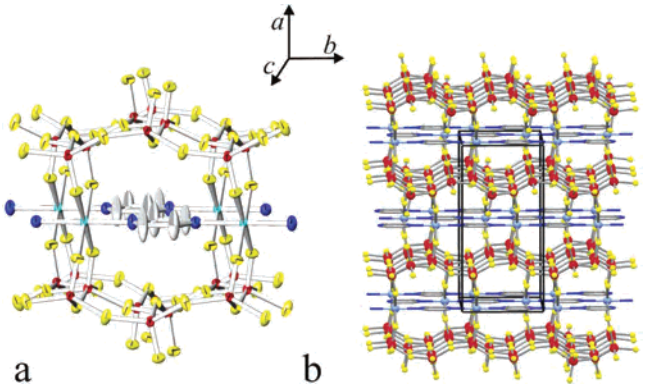


**Figure 1.** ∼[001] view of the structure of $Co(pyz)V_4O_{10}$ drawn with (a) 83% thermal ellipsoid probabilities and (b) showing the extended layered structure with the unit cell. Red = V, yellow = O, dark blue = N, light blue = Co, Ni, or Zn, white = C.

The vanadate layer, shown in Figure 2a, is constructed from distorted $VO_5$ square pyramids, each with one short V−O apical bond distance of ∼1.64 Å and four longer V−O basal bond distances of ∼1.80−2.01 Å. The distorted square pyramids share edges and form infinite zigzag chains down the *b* axis, Figure 2a, and which are in turn corner-connected to neighboring zigzag chains and form the resulting $V_4O_{10}^{2-}$ layers. The apical oxygen atoms alternate in an 'up−up−down−down' pattern down the edge-shared zigzag chains. This pattern of the apical oxygens matches the repeat unit of the $M(pyz)^{2+}$ chains, such that each M atom bonds to two 'up' oxygens from the oxide layer and the pyrazine resides in the space vacated by two 'down' oxygen atoms. The shortest V−V distances occur down the edge-shared zigzag chains at 3.03−3.06 Å (×2; Zn < Co < Ni), with an alternation between slightly longer (∼3.06 Å) and shorter

(28) Whangbo, M.-H. *Structure and Molecular Orbital Analyzer (SAMOA)*; North Carolina State University: Raleigh, NC, 2001.
(29) Hoffmann, R. *J. Chem. Phys.* **2005**, *44*, 5042.
(30) Koo, H.-J.; Whangbo, M.-H. *Solid State Commun.* **1999**, *111*, 353.

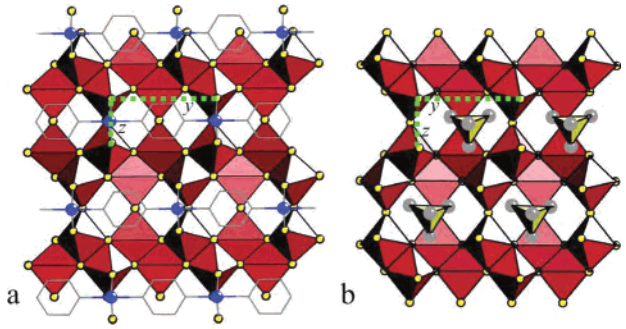


**Figure 2.** Sections of the $V_4O_{10}^{n-}$ layers in (a) Co(pyz)$V_4O_{10}$ and (b) $[N(CH_3)_4]V_4O_{10}$. Repeat distances between apical oxygen atoms are labeled as dashed green lines and are *y* (a, 7.00 Å; b, 6.64 Å) and *z* (a, 3.03 Å; b, 3.23 Å); Red polyhedra are $VO_5$, blue = Co, yellow = O, gray = C.

(~3.03 Å) V−V distances. This pattern suggests that possible electron localization at lower temperatures (see below) might involve further displacements of these alternating V−V distances. The V−V distances are a longer 3.36−3.38 Å (Ni < Co < Zn) between the vertex-shared $VO_5$ pyramids. A similar vanadate layer is found in $[N(CH_3)_4]V_4O_{10}$,[22] drawn in Figure 2b, and exhibits relatively longer V−V distances of 3.09−3.11 Å. However, the vanadate layer in this structure is reduced by one fewer electron and contains interlayer $N(CH_3)_4^+$ cations in equivalent positions as the pyrazine ligands in **I**−**III**. The repeat dimensions of the vanadate layer, marked *y* and *z* in Figure 2a and b, differ by a relatively small ~0.3 Å between these two structures, in comparison to the significantly larger interlayer distance found for $[N(CH_3)_4]V_4O_{10}$ (below).

The M(pyz)$V_4O_{10}$ structure can be envisioned as arising from an in situ intercalation and polymerization of cationic $M(pyz)^{2+}$ chains between the $V_4O_{10}^{2-}$ layers. The vanadate layers in **I**−**III** have the same connectivity of $VO_5$ polyhedra as found in $(C_7NH_{14})V_4O_{10}$[31] and $[N(CH_3)_4]V_4O_{10}$[22] but which contain organic interlayer cations and one less electron per $V_4O_{10}$ formula unit. The former exhibits metallic conductivity and shows evidence for the low-temperature ordering of $V^{4+}$ and $V^{5+}$. Two other hybrid structures that contain related vanadate layers are $(C_{12}H_{14}N_2)_{0.25}V_2O_5$ and (4-$H_2N-C_5H_5$-NH)$V_2O_5$.[32,33] These vanadate layers share the same general topology as in **I**−**III**, but the relative orientations of the $VO_5$ polyhedra in the zigzag chains alternate in an 'up−down−up−down' fashion rather than in the 'up−up−down−down' pattern. The layers in these are also reduced by only one electron per $V_4O_{10}$ formula unit and contain only organic interlayer cations. The addition of an interlayer transition metal, as found in **I**−**III**, doubles the cationic layer charge density to +0.050/Å$^2$ and requires the reduction of $V_4O_{10}^{n-}$ by one extra electron ($n$ = 1 to 2) to maintain an anionic charge density match of −0.050/Å$^2$. No other hybrid vanadate structures are currently known containing a similarly reduced vanadate layer of this type.

A bond-valence analysis was performed to obtain an estimate of the formal valence of vanadium in each structure,[34,35] and the results are listed in Table 3 as $\Sigma S_{ij}$(V). Bond valence calculations were performed using the respective V−O distances and $R^0$ values for $V^{5+}$ and $V^{4+}$ individually, as V has an average valence of 4.5+ in **I**−**III** and of 4.75+ in $[N(CH_3)_4]V_4O_{10}$. In **I**−**III**, the vanadium valence is calculated at +4.4 and +4.7 using $R^0$ for $V^{4+}$ and $V^{5+}$, respectively, in agreement with that expected for a formal oxidation state of +4.5. Further, the valence of V in $[N(CH_3)_4]V_4O_{10}$ is calculated by similar procedures to be +4.8 and +5.0, in comparison to +4.75 expected from the chemical formula. These oxidation states are consistent with two electrons per four vanadium atoms in the $V_4O_{10}^{2-}$ layers of **I**−**III** and with a single electron per four vanadium atoms in $V_4O_{10}^{1-}$. In addition, this is consistent with the relatively shorter V−V distances observed in the more-reduced M(pyz)-$V_4O_{10}$.

**Electrical and Magnetic Properties.** The existence of only one V site in these materials implies an average oxidation state of +4.5 and two unpaired electrons per $V_4O_{10}^{2-}$ unit. There are two limiting possibilities, randomly localized or fully delocalized electrons within the $V_4O_{10}^{2-}$ layers. The latter would result in a temperature-independent Pauli contribution to the susceptibility, while a Curie−Weiss contribution would be expected from the former, at least at high temperatures. Magnetic susceptibilities for each material are shown in Figure 3. Clearly, for all compounds one sees a strong temperature dependence, even for Zn(pyz)$V_4O_{10}$, which is consistent with the randomly localized model. The data in Figure 3 were also analyzed using the Curie−Weiss (C−W) model, and the results are collected in Table 4. The magnetic data for **III**, Zn(pyz)$V_4O_{10}$, appeared to follow the Curie−Weiss law only at high temperatures, and thus the extracted parameters should be viewed with caution as the values varied strongly with the choice of fitting range. Nonetheless, for **III** the observed Curie constant is consistent with two randomly localized $S = {}^1/_2$ spins per $V_4O_{10}^{2-}$ unit and the Weiss temperature suggests a predominant antiferromagnetic exchange. A reasonable Curie constant for **II**, Ni(pyz)$V_4O_{10}$, could only be found by inclusion of a temperature-independent paramagnetism (TIP) term due to a curvature in the $\chi^{-1}$ versus $T$ plot. This can be justified only if the curvature is due to a single-ion effect such as a van Vleck contribution, and such is often the case with $Ni^{2+}$ compounds in the paramagnetic regime.[36] The data for **I**, Co(pyz)$V_4O_{10}$, showed the best fit to the C−W law as evidenced by the precision of the extracted parameters. The large value of the observed Curie constant relative to the spin-only value is typical of $Co^{2+}$ in an octahedral site and results from spin−orbit coupling effects.[36] Note the small, positive values of $\theta_c$ for both **I** and **II** (M = Ni and Co) which indicate the presence of ferromagnetic exchange

(31) Riou D.; Roubeau, O.; Bouhedja, L.; Livage, J.; Férey, G. *Chem. Mater.* **2000**, *12*, 67.
(32) Bose, A.; He, P.; Liu, C.; Ellman, B. D.; Twieg, R. J.; Huang, S. D. *J. Am. Chem. Soc.* **2002**, *124*, 4.
(33) Shan, Y.; Huang, R. H.; Huang, S. D. *Angew. Chem., Int. Ed.* **1999**, *38*, 1751.
(34) Brown, I. D.; Altermatt, D. *Acta Crystallogr.* **1985**, *B41*, 244. Brese, N. E.; O'Keefe, M. *Acta Crystallogr.* **1991**, *B47*, 192.
(35) Hormillosa, C. *Bond Valence Calculator*, Version 2.00; McMaster University: Hamilton, Ontario, Canada, 1993.
(36) Mabbs, F. E.; Machin, D. J. *Magnetism and Transition Metal Complexes*; Chapman and Hall, London, 1973.

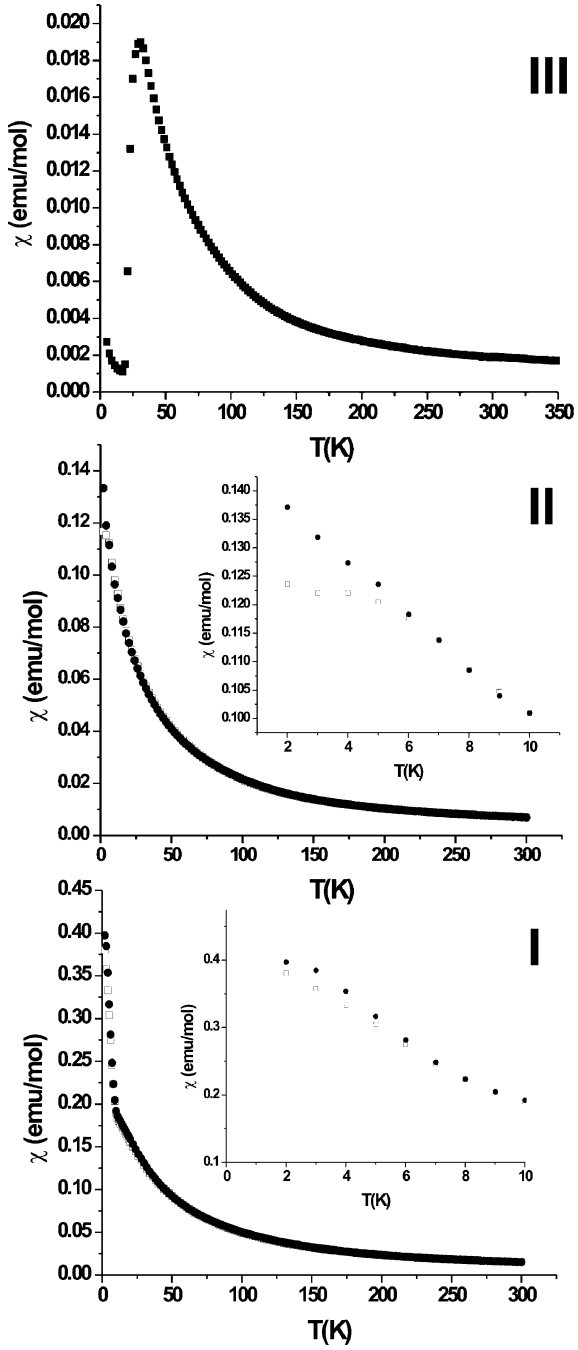


**Figure 3.** Magnetic susceptibility versus temperature for M(pyz)$V_4O_{10}$, M = Co (**I**), Ni(**II**), and Zn(**III**). The measuring field was 0.1 T. There was no difference between the zfc (□) and fc (●) data for the M = Zn material. The insets show a small zfc/fc divergence for both the M = Ni and Co compounds at low temperature.

**Table 4.** Results of Curie−Weiss Fits for Magnetic Susceptibilities of M(pyz)$V_4O_{10}$

| M | fitting range (K) | $C_{obs}$[a] | $C_{s.o.}$ | $\theta_c$(K) | TIP (emu/mol) |
|---|---|---|---|---|---|
| Zn | 225−350 | 0.79(2) | 0.75 | −118(10) | − |
| Ni | 100−300 | 1.72(3) | 1.75 | 17(2) | $9.7 \times 10^{-4}$ |
| Co | 100−300 | 4.302(4) | 2.62 | 15.7(2) | − |

[a] The units for $C$ are emu/mol·K.

correlations in both. Further evidence for the importance of short-range ferromagnetic correlations is seen in Figure 4 in $\chi T$ vs $T$ plots. In all cases, including for **III**, $\chi T$ increases

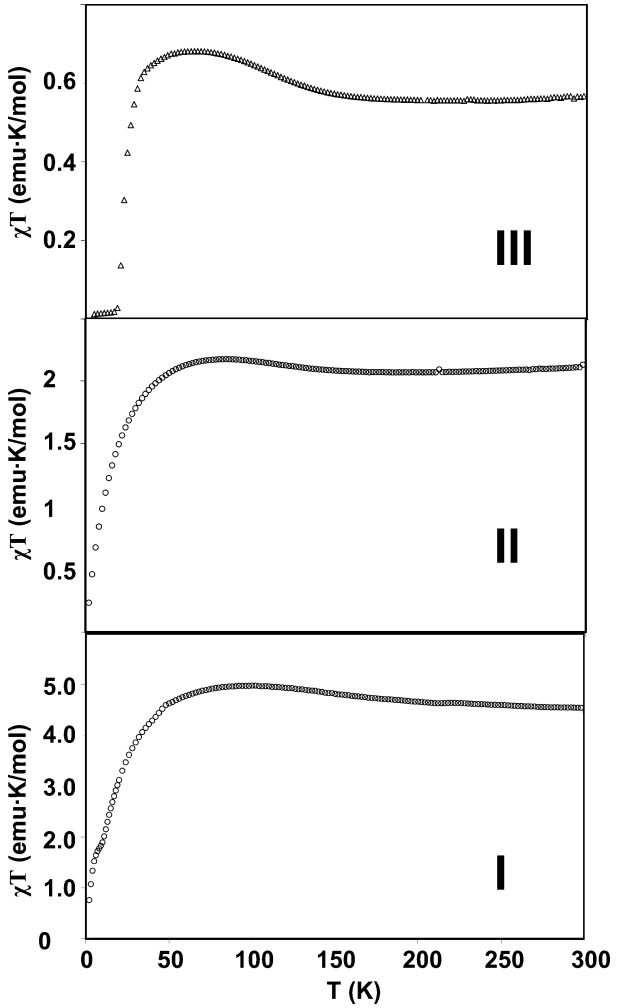


**Figure 4.** Plots of $\chi T$ versus $T$ for M(pyz)$V_4O_{10}$, M = Co (**I**), Ni(**II**), and Zn(**III**).

over some temperature range before decreasing at lower temperatures. This behavior indicates that both ferromagnetic and antiferromagnetic spin correlations are present in all three materials, a condition which would lead to spin frustration. Note that $\chi T$ for **III** approaches 0.6 emu/mol·K at the highest temperatures measured here, which is close to the expected value of 0.75 emu/mol·K for two $S = {}^1/_2$ spins per $V_4O_{10}{}^{2-}$ unit.

The most remarkable result is obtained for Zn(pyz)$V_4O_{10}$, where the susceptibility decreases abruptly below about 23 K to nearly zero, indicating the presence of a spin gap in this material. The low-temperature upturn below 15 K, evident in Figure 3, was fitted to a C−W expression and yielded the parameters $C = 0.0912$ emu/mol·K and $\theta_c = -2.1$ K. The fit was excellent, requiring no additional TIP term. This contribution was subtracted from the raw data and plotted in Figure 5, which provides unequivocal evidence for the presence of a singlet ground state and the formation of a spin gap. The inset of Figure 5 shows the so-called Fisher heat capacity, d($\chi T$)/d$T$, which indicates a phase transition at 22(1) K.[37] Without further structural information, it is difficult to speculate about the nature of this transition,

(37) Fisher, M. E. *Philos. Mag.* **1962**, *7*, 1731.

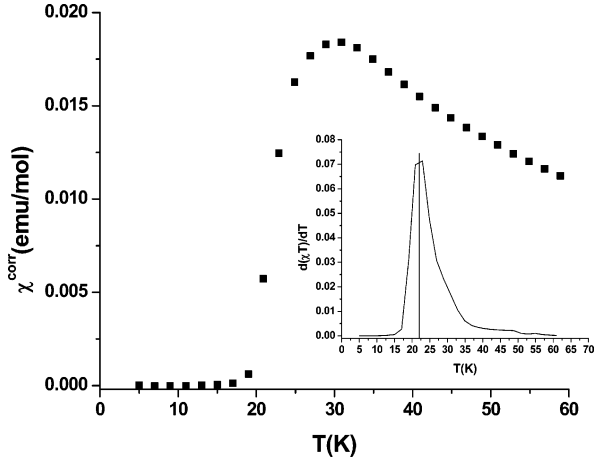


**Figure 5.** Magnetic susceptibility for $Zn(pyz)V_4O_{10}$, corrected by subtraction of the low-temperature Curie−Weiss tail (see text). The inset shows the Fisher heat capacity, which indicates a phase transition at 22(1) K.

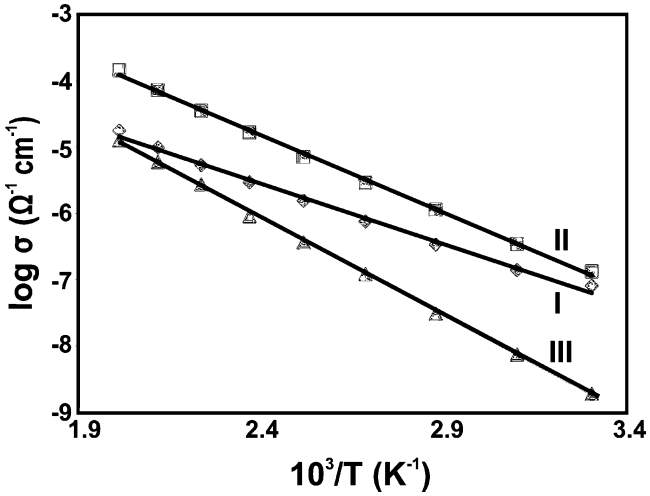


**Figure 6.** Electrical conductivity data for $M(pyrazine)V_4O_{10}$ for M = Co (**I**), Ni (**II**), and Zn (**III**), plotted as log $\sigma$ versus $1/T$.

but it seems clear that some form of $V^{4+}/V^{5+}$ charge ordering could play a role.

Of course, other vanadate materials displaying a spin gap are known, for example $NaV_2O_5$, $MgV_2O_5$, and $CaV_2O_5$.[16] There are important differences between $Zn(pyz)V_4O_{10}$ and these compounds, however. First, while the structure of the vanadate layers is similar, i.e., both contain chains of corner-shared square pyramids that condense via edges to form the zigzag chains, there are some subtle differences. As shown previously in Figure 2, within the double chains of the $V_4O_{10}^{2-}$ layer, the orientation of the square pyramid apex alternates 'up−down−up−down' along the corner-shared chains, while for the other materials mentioned, the apex orientation is the same, either up or down along the individual chains. This will have an influence on the magnetic exchange within the layers.[38] Second, for $Zn(pyz)V_4O_{10}$, there is no evidence for antiferromagnetic short-range correlations at temperatures above the spin-gap transition. For example, in $NaV_2O_5$, one-dimensional antiferromagnetic correlations are observed in the form of a broad maximum near 300 K while the spin gap transition is at 35 K.[39] Attempts to fit the data of Figure 3 using $S = {}^1/_2$ short-range order models, such as the AF linear chain, dimer or even the square lattice were not successful. Finally, the introduction of magnetic ions, such as $Ni^{2+}$ and $Co^{2+}$ into the sites between the $V_4O_{10}^{2-}$ layers destroys the spin gap state. The insets of Figure 3 for both materials show weak ZFC/FC divergences at temperatures below 10 K, which may indicate a spin glassy ground state, which would not be inconsistent with the observation of the coexistence of ferromagnetic and antiferromagnetic spin correlations. The Fisher heat capacity of both M = $Ni^{2+}$ and $Co^{2+}$ materials showed no sharp peaks, which again suggests that no long-range antiferromagnetic order is present in these materials down to at least 2 K. Clearly, much further low-temperature work, such as heat capacity, NMR, and neutron scattering, is needed to fully characterize these interesting materials.

The temperature-dependent conductivity of all three compounds, Figure 6, follows Arrhenius' law: $\sigma = \sigma_o \exp(-E_a/RT)$, with apparent activation energies of 0.36 (**I**), 0.46 (**II**), and 0.59 eV (**III**). These conductivity data suggest a greater tendency toward electron localization in $Zn(pyz)V_4O_{10}$, with perhaps a complete electron localization and $V^{4+}/V^{5+}$ ordering at 22 K giving rise to the spin gap. Both the magnitudes and temperature dependencies of the electrical conductivities are similar to that found in the related reduced $(C_7NH_{14})V_4O_{10}$,[31] which has a different repeating pattern of $VO_5$ square pyramids. The conductivity of $(C_7NH_{14})V_4O_{10}$ shows an apparent activation energy of 0.25−0.35 eV and a discontinuity at ∼230 K which is proposed to result from the onset of $V^{4+}/V^{5+}$ and quinuclidinium cation ordering within the interlayer spaces. These trends suggest that as yet unknown subtle structural and temperature dependencies strongly influence the electron localization and spin transitions in layered hybrid vanadates.

**Spin−Spin Interactions.** To help determine the type of spin lattice that leads to the spin gap for **III**, the spin-dimer analysis method was employed within the extended Hückel approximation.[28−30] In this approach, a relative measure of the antiferromagnetic spin-exchange interaction is obtained from the relationship: $J_{AF} \alpha -(\Delta e)^2$, where $\Delta e$ is the energy separation between two interacting atomic orbitals with parallel or antiparallel spin arrangements. The lowest-lying d orbital for **I**−**III** is $d_{xy}$ and can be either singly occupied or empty. Because there is only one unpaired spin per two V in the $V_4O_{10}^{2-}$ formula, the 'spin monomers' are either edge-shared $V_2O_8^{7-}$ or corner-shared $V_2O_9^{9-}$ clusters. The calculated $\Delta e$ values for the four different clusters of adjacent $VO_5$ square pyramids are given in Table 5 and Figure 7a (1−4). The $\Delta e_3$ interaction for the corner-shared $V_2O_9^{9-}$ cluster is the largest at ∼500 meV, and therefore, its bonding $\psi$ is the lowest lying and singly occupied. Between adjacent $V_2O_9^{9-}$ clusters there are three types of spin dimer interactions, labeled as interactions 5−7 in Figure 7a. The largest interaction energy occurs for $\Delta e_5$ at ∼149 meV and which favors an antiparallel spin alignment between these adjacent clusters and leads to the spin lattice shown in Figure 7b.

(38) Whangbo, M.-H.; Koo, K.-J.; Dai, D. *J. Solid State Chem.* **2003**, *176*, 417.
(39) Isobe, M.; Ueda, Y. *J. Phys. Soc. Jpn.* **1996**, *65*, 1178.

**Table 5.** Calculated Interaction Energies, $\Delta e$ (meV), in M(pyz)$V_4O_{10}$[a]

| M | $\Delta e_1$ | $\Delta e_2$ | $\Delta e_3$ | $\Delta e_4$ | $\Delta e_5$ | $\Delta e_6$ | $\Delta e_7$ |
|---|---|---|---|---|---|---|---|
| Zn | 3 | 47 | 502 | 91 | 149 | 0.7 | 22 |
| Ni | 20 | 43 | 500 | 87 | 144 | 9 | 21 |
| Co | 12 | 46 | 503 | 84 | 139 | 4 | 22 |

[a] The $\Delta e$ subscripts are numbered according to the interactions labeled in Figure 7a.

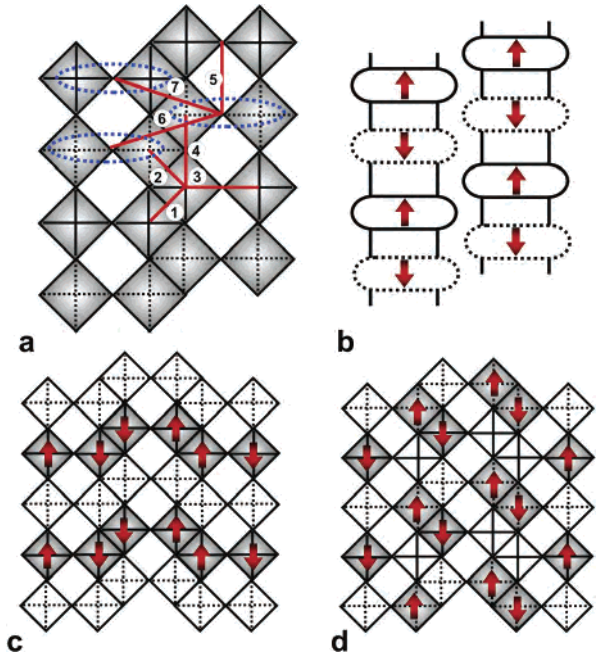


**Figure 7.** (a) $V_4O_{10}^{2-}$ layer and six possible spin-dimer interactions (1,2 − $V_2O_8^{8-}$; 3,4 − $V_2O_9^{10-}$; 5,6,7 − $V_4O_{16}^{-14}$); (b) the predicted spin lattice based on strongly interacting $V_2O_9^{9-}$ clusters; and two possible spin lattices for the charge localization of $V^{4+}$ sites (shaded) exhibiting (c) both ferromagnetic and antiferromagnetic or (d) only antiferromagnetic $V^{4+}$−$V^{4+}$ interactions.

This spin lattice is closely analogous to that calculated for α-$NaV_2O_5$,[30,40] which has $V_2O_9^{9-}$ clusters that form the 'rungs' of a ladder with a larger rung-to-rung interaction energy of 259 meV and a higher transition temperature of 35 K. This larger interaction likely owes to the apical O atoms in the ladder oriented in an all-up or all-down fashion but which for **III** alternate in an up-and-down pattern down the ladder. Also of note in the proposed spin lattice of Figure 7b is that there are ferromagnetic rung-to-rung interactions for a near degenerate $\Delta e_6$ (0.7 meV) and antiferromagnetic rung-to-rung interactions for $\Delta e_7$ (22 meV). The smaller V−O−V angle of 101.86(9)° would also tend toward a weak ferromagnetic coupling.[41] Thus, unlike in α-$NaV_2O_5$, the interaction energies here suggest the possibility of the coexistence of both ferromagnetic and antiferromagnetic exchange within a triangular spin arrangement, a condition that typically leads to spin frustration. The charge localization of the $V^{4+}$ sites could lead to ordered superstructures showing both ferromagnetic and antiferromagnetic spin interactions, such as in Figure 7c, or to only antiferromagnetic interactions as in Figure 7d (as proposed for α-$NaV_2O_5$).

Additional magnetic $Co^{2+}$/$Ni^{2+}$ ions occur on the pyrazine-bridged chains for **I** and **II**, which coordinate to every other pair of O apexes of the $V_2O_9^{9-}$ rungs, e.g., either all dashed or all solid ellipses in Figure 7b. Extended Hückel calculations indicate mixing of the $d_{x^2-y^2}$ and $d_{z^2}$ orbitals of $Ni^{2+}$/$Co^{2+}$ with the orbitals containing $d_{xy}$ of V; a molecular orbital picture of this is given in the Supporting Information. However, late transition metals bridged by pyrazine ligands normally exhibit antiferromagnetic exchange[42] which would be in conflict with the spin lattice of Figure7b because the set of either all-up or all-down $V_2O_9^{9-}$ clusters have a single spin orientation. This would result in alternating in-phase and out-of-phase combinations of $d_{xy}$ with $d_{z^2}$/$d_{x^2-y^2}$ orbitals and would possibly suppress the spin-gap transition observed for **III**.

**Thermal Structure Evolution.** Hybrid oxides/organics containing pyrazine can undergo ligand loss at relatively low temperatures. Examples include pyrazine loss from $AgReO_4$(pyrazine) or $Ag_3Mo_2O_4F_7$(pyrazine) at 150 °C[15] or from $MoO_3$(pyrazine)$_{0.5}$ at 320 °C,[43] each of which are pyrazine-pillared layered structures and yield condensed oxides upon removal of the pillars. However, the structural role of pyrazine in the M(pyrazine)$V_4O_{10}$ structures is not as a pillar and, upon removal, could lead to microporosity owing to the relatively large cavities in which the pyrazine molecules reside, Figure 1a. The accessibility of the interlayer spaces to different small molecules would allow future investigations into the effect that small structural changes have on the magnetic and electrical properties. Measurements of the weight losses and concomitant structural changes during heating were performed on pure samples, including TGA for **I**−**III** and TGA−MS, PXRD, and SEM for **I** and **II**.

**Thermogravimetric Analysis (TGA).** Each sample was heated to 700 °C under flowing $N_2$ or $O_2$, and the weight losses plotted as a function of temperature, panels a and b of Figure 8, respectively. Under flowing $N_2$, all three exhibit a single sharp weight loss (27.0% for **I**, 27.3% for **II**, and 27.0% for **III**) in the temperature range of 500−575 °C. A very small weight loss of ∼1.6% is also observed at ∼400 °C for **I** and **III**. This total combined weight loss is significantly greater than that expected for the loss of pyrazine alone (calcd 15.9% for **I** and **II** and 15.7% for **III**). A PXRD analysis of the TGA products revealed a mixture of $V_2O_3$ and $Co_2VO_4$ for **I**, $V_2O_3$ and Ni for **II**, and $V_2O_3$, Zn, and $ZnV_2O_4$ for **III**, which are all well-reduced metal oxides containing $V^{3+}$ ions. The vanadate layer, as well as $Ni^{2+}$ and $Zn^{2+}$, has likely been reduced by a reaction with the pyrazine ligand at high temperatures (see TGA−MS below). For every oxygen lost per formula unit via reaction with the ligand, the valence of vanadium decreases by +0.5, e.g., from $V^{4.5+}$ in $V_4O_{10}^{2-}$ to $V^{4+}$ in $V_4O_9^{2-}$ to $V^{3.5+}$ in $V_4O_8^{2-}$ to $V^{3+}$ in $V_4O_7^{2-}$, etc. The calculated weight loss of one pyrazine ligand and 3.5 oxygen atoms per formula unit matches reasonably well (calcd 27.0%) with the experimental weight losses.

(40) Whangbo, M.-H.; Koo, H.-J.; Lee, K.-S. *Solid State Commun.* **2000**, *114*, 27.
(41) Hay, P. J.; Thibeault, J. C.; Hoffmann, R. *J. Am. Chem. Soc.* **1975**, *97(17)*, 4884.
(42) Jimbo-Kobayashi, A.; Kobayashi, A.; Tamura, I.; Kawada, N.; Miyamoto, T. *Bull Chem. Soc. Jpn.* **2005**, *78*, 445.
(43) Xu, Y.; Lu, J.; Goh, N. K. *J. Mater. Chem.* **1999**, *9*, 1599.

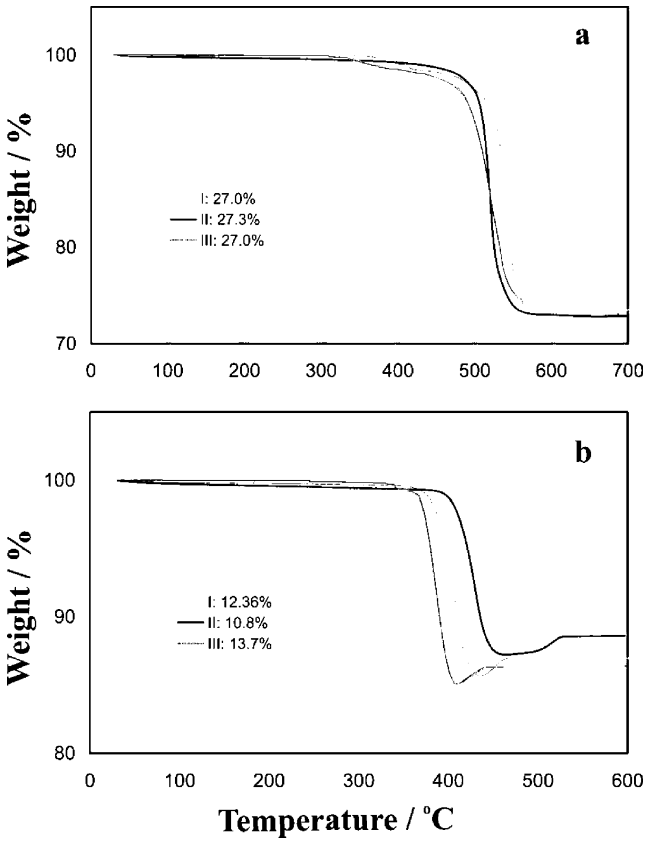


**Figure 8.** Thermogravimetric analyses of M(pyz)$V_4O_{10}$ for M = Co (**I**), Ni (**II**), and Zn(**III**) under flowing (a) nitrogen and (b) oxygen.

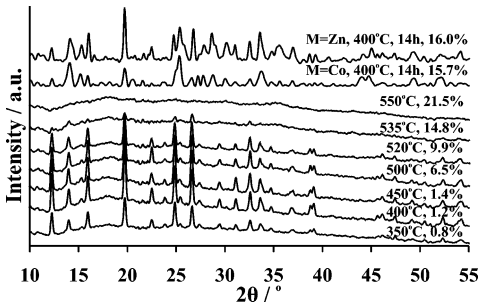


**Figure 9.** Powder X-ray diffraction patterns of Co(pyz)$V_4O_{10}$ as a function of temperature and weight loss. The two uppermost diffraction patterns are obtained from finely ground Co(pyz)$V_4O_{10}$ and Zn(pyz)$V_4O_{10}$ samples heated to 400 °C for 14 h.

Under flowing $O_2$, all three exhibit a single-step weight loss at the relatively lower temperature range of 380−420 °C, Figure 8b, but which is followed concomitantly by a single-step weight gain. The PXRD of the TGA residues after heating to 600 °C revealed a mixture of $V_2O_5$, MO, and $MV_2O_6$ for **I** and **II** (M = Co and Ni, respectively) and a mixture of $V_2O_5$ and $ZnV_2O_6$ for **III**. Thus, the weight losses can be attributed to the initial removal/decomposition of the pyrazine ligands and the subsequent weight gains arising from the oxidation of $V^{3+/4+}$ to $V^{5+}$ under flowing $O_2$ gas. The gain of one oxygen atom per formula unit (e.g., $V_4O_{10}^{2-}$ to $V_4O_{11}^{2-}$) corresponds to only $V^{5+}$ cations. Thus, the observed total weight losses (12.4% for **I**, 10.8% for **II**, and 13.7% for **III**) agree reasonably well with the calculated weight loss for the removal of one pyrazine molecule and gain of one oxygen atom per formula (calcd 12.7% for **I** and **II** and 12.6% for **III**). The smaller weight loss observed for **II** (∼2% less) may arise from the more complete reduction of $Ni^{2+}$ to Ni metal by pyrazine but which is not readily reoxidized to NiO.

**Mass Spectroscopy (TGA−MS).** To identify the major products liberated during the TGA heating of **I** and **II**, tandem TGA−MS experiments were performed. Under flowing $N_2$, the TGA−MS data for **I** show that $CO_2$ is the major component lost at ∼500 °C along with detectable amounts of pyrazine and pyrazine fragments. Also, $O_2$ begins to be liberated in significant amounts at 600 °C (see Supporting Information). The former weight loss is that expected from the removal of intact pyrazine, as well as through reaction with the vanadate layer to give $CO_2$ (e.g., $Co(C_4H_4N_2)V_4O_{10} \rightarrow CoV_4O_{10-x} + CO_2 +$ fragments), while the latter weight loss at higher temperatures arises from further autoreduction to yield $V_2O_3$. The pyrazine nitrogen atoms are either removed as part of the pyrazine or fragments or become incorporated in the products as dopant impurities. The small ∼1.6% weight loss at 400 °C arises from the liberation of $O_2$ as the major component and is seemingly reversible with a currently unknown reaction/product. For **II**, the TGA−MS data show that $CO_2$ is the major component lost at ∼500 °C along with only faint amounts of pyrazine fragments, while $O_2$ is the major component lost beginning at just under 600 °C. These results are closely analogous to those for **I**, with the weight losses at 500 °C attributed to the liberation of reaction products between the pyrazine ligands and the vanadate layers. The weight loss at 600 °C arises from autoreduction of the sample to give $V_2O_3$ and Ni.

**Powder X-ray Diffraction (PXRD) and Scanning Electron Microscopy (SEM).** The pyrazine and pyrazine fragments detected in the TGA−MS of **I** indicate the possible formation of new crystalline and/or microporous structures. The PXRD of **I** (not ground) was measured after heating to increasing temperatures from 400 to 600 °C, Figure 9. The diffraction patterns show the solid remains crystalline at up to 520 °C, even with a 9.9% weight loss. At higher temperatures, the solid becomes amorphous, with combined weight losses of 14.8% by 535 °C and 21.5% by 550 °C, which exceeds the weight loss expected from pyrazine alone (calcd 15.9%). Smaller weight losses occur at lower temperatures, including 0.8%, 1.2%, 1.4%, and 6.5% for 350, 400, 450, and 500 °C, respectively. These data suggest the possibility of micropore formation in the cavities vacated by pyrazine, Figure 1a. To shorten the diffusion pathway of pyrazine leaving the crystal and to reduce its reactivity with the vanadate layer, samples of **I**−**III** were ground into a fine powder and the TGA and PXRD experiments were repeated. By heating to just 400 °C for 14 h, the samples exhibit a slow weight loss which reaches 15.7−16.0 wt %, in agreement with the 15.9 wt % expected by the loss of pyrazine alone. Thus, the reaction between the pyrazine ligands the vanadate layers is avoided. In addition, the crystallinity of **I** and **III** is preserved, as shown plotted in the upper diffraction patterns of Figure 9. There is a

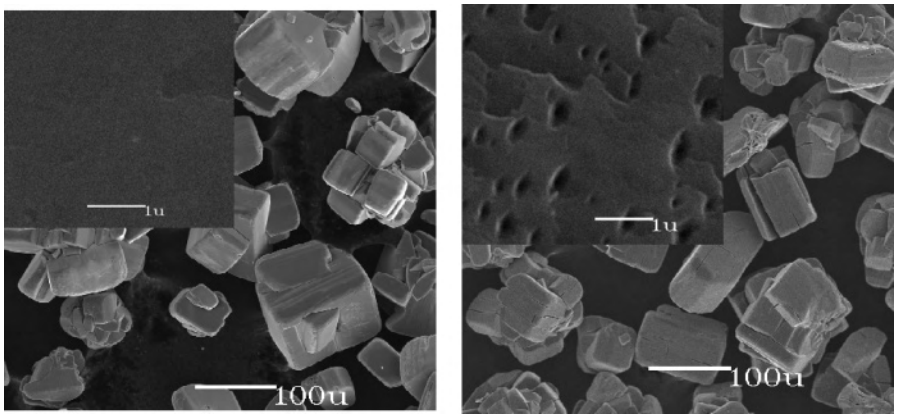


**Figure 10.** SEM images of selected surfaces of $Co(pyz)V_4O_{10}$ both before (a) and after (b) heat treatment at 600 °C under flowing $N_2$.

noticeable shift in the diffraction peaks and which are relatively broad and has so far prevented a detailed indexing and refinement of the resulting structures.

Surprisingly, at even up to 550−600 °C and with substantial loss of pyrazine (up to 21 wt %) large single crystals of **I** appear unchanged and retain their size, morphology, and reflective and smooth surfaces. However, these do not exhibit indexable single-crystal X-ray diffraction. At ∼540 °C, an SEM analysis of **I** shows that ∼15−30% of the crystals exhibit a small amount of surface cracking, and the remaining crystals show no detectable morphological changes or macropore formation. The full SEM results of **I** and **II** are given in the Supporting Information. An SEM analysis of **I** after heating to 600 °C, Figure 10, exhibits substantial surface cracking and pitting/macropores of the surfaces of ∼10−20% of the sample. These changes likely represent the beginning of long-range structural collapse and condensation of the smaller micropores within the crystal, the latter of which exist only at the lower temperatures.

## Conclusions

Three new reduced hybrid vanadates, $M(pyz)V_4O_{10}$ (M = Co, Ni, Zn), were prepared under hydrothermal conditions and contain reduced $V_4O_{10}^{2-}$ layers that are coordinated to layers of $M(pyz)^{2+}$ chains. Magnetic susceptibilities show a transition to a spin-singlet ground state and the formation of a spin-gap below 22(1) K for **III** but which is not observed for either **I** or **II**. Evidence for both ferromagnetic and antiferromagnetic spin correlations is found for all three, consistent with the spin lattice proposed from spin-dimer analysis calculations. The temperature-dependent electrical conductivities show apparent activation energies of 0.36 (**I**), 0.46 (**II**), and 0.59 eV (**III**). The solids decompose beginning at ∼500 °C under flowing $N_2$ with the liberation of pyrazine, pyrazine fragments, and $CO_2$ via reaction between the pyrazine and the vanadate layer. For finely powdered samples of **I** and **III**, the crystallinity can be maintained with the total loss of pyrazine at 400 °C, owing to a shortening of the diffusion pathway which suppresses the reaction with the vanadate layer. At higher temperatures of 600−800 °C, all three decompose to parent oxides under flowing $O_2$ or to reduced metal oxides under flowing $N_2$. Thus, these new reduced layered vanadates have revealed unique and rich new avenues of investigation for hybrids, including both a remarkable magnetic transition and low-temperature ligand removal, leading either to well-reduced solids or potentially to microporosity, and should be a source of much future research.

**Acknowledgment.** Assistance with single crystal X-ray data (Paul Boyle) and TGA−MS (Joel Miller), and support from a Beckman Young Investigator Award from the Beckman Foundation (P.A.M.), an ACS-PRF grant (40963-G10), and NCSU startup funds (P.A.M.). Natural Sciences and Engineering Research Council of Canada for a Discovery Grant (J.E.G.), a predoctoral fellowship (A.S. Sefat) and a Major Facilities Access Grant for the Brockhouse Institute for Materials Research.

**Supporting Information Available:** Crystallographic data in CIF format, complete data for TGA−MS, SEM, PXRD of products from thermogravimetric analysis, and an MO picture of a '$NiV_4O_{18}$' fragment showing the interaction between V $d_{xy}$ with Ni $d_{x^2-y^2}/d_{z^2}$ orbitals. This material is available free of charge via the Internet at http://pubs.acs.org.

IC0604563